RSC Advances

ROYAL SOCIETY OF CHEMISTRY

www.rsc.org/advances

RSC Advances

RSCPublishing

ARTICLE

45S5 Bioglass Analogue reinforcing Akermanite Ceramic Favorable for Additive Manufacturing Mechanically Strong Scaffolds

Cite this: DOI: 10.1039/x0xx00000x

Received 00th January 2012,
Accepted 00th January 2012

DOI: 10.1039/x0xx00000x

www.rsc.org/

Xiaoqing Wang[a], Lei Zhang[a], Xiurong Ke[a], Juncheng Wang[a], Guojing Yang[a]*, Xianyan Yang[b], Dongshuang He[b], Huifeng Shao[c], Yong He[c], Jianzhong Fu[c], Sanzhong Xu[a], and Zhongru Gou[b]*

Calcium-magnesium silicate bioceramics have been attracted increased interest in developing porous scaffolds for bone tissue engineering applications, mainly due to their excellent bioactivity and ability to bond to hard tissues. However, the shaping of these bioceramics into complex porous constructs is challenging, and especially the conventional high temperature pressureless sintering is not always effective to improve its mechanical properties, but furthermore compromise its biologically relevant performances. Here we developed a low melt-point bioactive glass (BG)-assisted sintering approach to improve the mechanical properties of the akermanite ceramics with and without intentionally manufacturing macropore structures. The experimental results indicated that the 4 wt% B_2O_3-containing 45S5 BG analogue could readily reinforce the akermanite ceramics at 20~40 wt% content and a material extrusion 3D-printing followed by pressureless sintering process could be employed to fabricate high-strength porous scaffolds with ten times higher compressive strength (~36 MPa) than the pure akermanite porous ceramic. Moreover, the composite porous ceramics showed slower biodegradation in Tris buffer *in vitro* but not heavily affect the strength of its porous formulation for a long time stage (6 weeks). It is proposed that the 3D printing followed by NCS-B-assisting sintering process represents an effective alternative for developing high strength bioceramic scaffolds potentially for repair of load-bearing segmental bone defects.

1. Introduction

For bone defect repair, the favorable mechanical strength, excellent bioactivity and controlled degradation of porous biomaterials are needed to meet different clinical requirements. Calcium phosphates (CaPs) such as hydroxyapatite (HA) and biphasic calcium phosphate (BCP) of HA/β-tricalcium phosphate (β-TCP), have been widely used in synthetic bone replacement due to their chemical similarity to bone mineral. *In vivo* and *in vitro* studies have reported that CaPs, no matter in which form (bulk, coating, or porous) or phase (crystalline or amorphous) that are in, consistently support the attachment, proliferation, and differentiation of osteoblasts. However, clinical investigation has demonstrated that the porous BCP and HA are virtually inert, remaining in body for 3 to 7 years post-implantation[1,2,3]. This should make BCP and HA less favored as scaffold material for use in bone tissue engineering.

The bioactivity of bioglasses (BGs) and glass-ceramics (GCs) is attributed to the formation of a bone-like carbonated hydroxyapatite (CHA) layer on their surface. BGs and GCs of specific compositions have been studied for over four decades since the milestone formulation of Hench's 45S5 Bioglass® has shown to directly bond to bone mineral[4]. The ability of 45S5 BG to enhance bone growth has been widely assessed, due to a possible effect on the gene expression of osteobastic cells[5]. Some attempts have also confirmed that BGs can be used as sintering aids to improve the mechanical and biological performances of the bioceramics. Winkel et al.[6] developed a 13-93 BG reinforced HA ceramic sintering at a low temperature, and obtained oriented pore composite scaffolds. Lin et al. prepared the 45S5 BG-reinforced wollastonite porous ceramics which showed appreciable compressive strength (~109 MPa) at nearly 50% of open porosity when sintering at 1100°C[7,8]. However, the high strength of the later was sacrificed with the porosity, and the low biodegradation nature of the former also limit its applications. In particular, the *in vivo* studies have showed that overfast degradation of wollastronite scaffolds may not match with new bone ingrowth during bone defect repair[9].

Calcium-magnesium silicate ceramics, have received increased interest due to their desirable bioactivity[10]. It is studied that akermanite ($Ca_2MgSi_2O_7$) ceramic is bioactive[11],

and the *in vitro* studies[12] and *in vivo* evaluation in animal models[13] have displayed better activities of proliferation and osteogenesis on akermanite ceramic than on the clinically available β-TCP. Hence, it can be assumed that a suitable combination of akermanite with an appropriate BG to produce the porous formulation of their composites might render greater mechanical and biological functions compared to them alone.

On the other hand, the shaping of bioceramics into complex structures is challenging, especially for developing porous scaffolds for bone tissue engineering. Traditional methods such as direct foaming and sacrificial templates have limited control over the shape and dimension of the individual pores[14], thus the simultaneous control of shape and properties is difficult. In contrast, additive manufacturing technology (AMT) offers the potential to precisely replicate a geometry directly from a bone defect by adding material in a layer-by-layer approach. AMT is particularly useful for the shaping of complex and porous structures for bone repair[15]. In the ceramic ink-based material extrusion 3D-printing system, the binder-pre-mixed ceramic ink is extruded through a micro-nozzle to form as filament and spread on the substrate, thus inscribing in the layer the corresponding cross-section of a 3D-model of the object to be built. Although this technique is simple and intriguing, the direct ceramic ink writing method is either confined to *pressureless compacting* and/or *pressureless sintering*, which impairs the densification and strength of pore struts[16]

Recently, we have designed a new *low-melt-point* BG, which showed highly bioactive and appreciable strength after sintering below 900°C[17]. The parent BG of such biomaterial was based on the composition of 45S5 Bioglass® and added with ~4% $\underline{B}_2O_3$ to form a $\underline{N}a_2O$–2$\underline{C}$aO–3$\underline{S}iO_2$-based BG (named as 'NCS-B'). Thus, such 45S5 BG analogue, would be a promising co-firer for reinforcing bioceramics. Based on this hypothesis, the objective of this study is to investigate the effect of NCS-B on the sintering, structural, mechanical, and *in vitro* biological properties of akermanite/NCS-B (porous) ceramics with varying biphasic percent ratio (hereafter denoted as AK*x*/ NCS-B*y*; *x*=100, 80, 60, 40; *y*=0, 20, 40, 60). The experimental results confirmed that the AK60/NCS-B40 porous ceramic possessed high strength and slower biodissolution *in vitro* in comparison with the pure akermanite, which may provide an insight into the design rule of the new porous bioceramics for large-area segmental bone defect repair.

2. Materials and Methods

2.1 Preparation of akermanite and NCS-B powders

The NCS-B ($CaO–SiO_2–Na_2O–P_2O_5–B_2O_3$) was prepared by using a melt-quenching method as described in our previous study[17]. Akermanite powders were prepared by a sol–gel process using tetraethyl orthosilicate ($(C_2H_5O)_4Si$, TEOS), $Mg(NO_3)_2·6H_2O$, and $Ca(NO_3)_2·4H_2O$ as start materials[11]. The powders were planetary milled for 4 h to form superfine particles (<2.0 μm). The thermograwimeteric and differential thermal analysis (TG/DTA) was carried out for the NCS-B powder on TG/ DTA6200 of TA Instruments with a 10°C·min^{-1} heating rate under an air atmosphere.

2.2 Preparation of AK*x*/NCS-B*y* GC composite samples

Cylindrical (Ø 6×2 mm, Ø 8×10 mm, Ø 25×4 mm) and cubic (45×8×6 mm) AK*x*/NCS-B*y* compacts with 0%, 20%, 40%, and 60% NCS-B were prepared with a pressure of 10 MPa (see Tab. 1). Specifically, the polyvinyl alcohol (PVA; ~6 kDa) solution (1.2% w/v) was prepared under magnetic stirring. Then the PVA solution was dispersed to the milled powders with a L/S mass ratio of 0.7:1. The pastes were kept at 60°C for 8 h. The compact samples were prepared using a uniaxial pressure in stainless steel moulds. Finally, the green compacts were sintered respectively at 1000°C−1150°C for 3 h in a muffle furnace with a heating rate of 3°C/min, and followed by cooling naturally. The phase of ceramics was examined in a Rigaku D/max-rA (Geigerflex) X-ray diffractometer (XRD) with a scanning rate of 0.02°·min^{-1}.

Table 1. The composition of starting materials and porosity of the sintered ceramics.

Samples	Composition		Porosity (%)			
	AK	NCS-B	1000°C	1050°C	1100°C	1150°C
AK100/NCS-B0	100	0	10.8±2.7	7.4±2.1	5.6±2.7	5.1±1.3
AK80/NCS-B20	80	20	6.5±1.6	2.7±0.8	2.2±1.1	2.5±1.7
AK60/NCS-B40	60	40	5.7±1.9	2.2±1.4	1.8±1.3	3.4±2.4
AK40/NCS-B60	40	60	3.4±1.2	3.0±2.4	3.5±2.6	4.6±2.6

2.3 Porosity test

Various heat treatment temperatures were considered and the densification of the ceramics was monitored by measuring the open pore porosity. The porosity was measured using a mercury porosimetry (AutoPore IV 9510). Hg intrusion volume during the high pressure loading phase was determined in cm^3 per unit sample weight.

2.4 Evaluation of mechanical properties

Compressive and flexural strength of the ceramics (*n*=8) were measured using a universal testing machine (Instron, Canton, MA) at a constant crosshead speed of 0.5 mm min^{-1}. The mechanical test follows the guidelines set in ASTM D5024-95a.

2.5 *In vitro* bioactivity assessment in SBF

The 1100°C-sintered samples (Ø 6×2 mm) were immersed in 8.0 ml SBF at 37°C and monitored the formation of CHA on the discs. After soaking for 1−7 d, the discs were washed with ethanol and observed using scanning electric microscopy (SEM; JEM-6700F, Japan), and a local chemical analysis was carried out by face-scanning energy dispersive X-ray (EDX). Prior to examination, the samples were coated with a thin layer of gold. All the immersion media were saved for inductively coupled plasma (ICP; Thermo) analysis of Mg, Si, B, Ca and P to measure ionic concentrations.

2.6 *In vitro* Biodissolution test

In order to evaluate the biodissolution *in vitro* (weight loss) of the ceramics, the discs (W0; Ø 25×4 mm) sintered at 1100ºC were immersed in 200 ml Tris buffer, with an initial pH 7.4 at 37°C, simulating the body's pH as a function of immersion time (up to 56 d). After immersing for every 3 d, 20% of supernatant was extracted for ICP-OES measurement and the equal volume of fresh buffer was added. The disc samples were rinsed with ethanol, and then dried up to mass constancy (Wt) before weighing. The weight decrease was expressed as the following equation: weight loss=Wt/W0×100%.

2.7 Material extrusion 3D printing of AK*x*/NCS-B*y* BGC scaffolds

It was taken into account the aggregation of the superfine AK*x*/NCS-B*y* powders in PVA solution, the homogenous AK*x*/NCS-B*y* ink was prepared by mixing 4 g of powder with 6.5(±0.2) g of aqueous carboxyl methyl cellulose solution (0.9 wt%). The printing device was based on a home-made three-axis positioning system. For layer-by-layer (LbL) ceramic ink writing of the scaffolds (~10×10×10 mm), the ceramic ink was added to a 5 ml syringe and extruded through a conical nozzle (400 μm) by the movement of a piston rod. A porous scaffold model with 3D periodic porous architecture was designed using software. The scaffolds using initial distance between green filaments were ~350 μm. The dosing pressure to the syringe pump was 0.95 bar and the moving speed of the dispensing unit was set to 3 mm s^{-1}. Obtained scaffolds were dried at 65°C, and then sintered respectively at 1050°C and 1100°C for 3 h using a heating rate of 2°C/min, and finally cooled naturally.

2.8 Statistical analysis

All the data above were expressed as mean ± standard deviation (SD) and analyzed with the one-way ANOVA. In all cases the results were considered statistically significant with a p-value less than 0.05.

3. Results

3.1 Thermal analysis of the NCS-B powder

According to the TG-DTA analysis (Fig. 1), the principal characteristic was the presence of an endothermic melting peak (T_m) at ~935°C for the NCS-B powder. The intensity of exothermal peaks for this BG was very high at 790~860°C, which could be attributed to the crystalline products of $Na_2Ca_2Si_3O_9$ and CaB_2O_4. Evidently, the former was consistent with the well-known crystalline phase of pure 45S5 BG.

3.2 Phase analysis of the AK*x*/NCS-B*y* ceramics

XRD analysis results for the AK*x*/NCS-B*y* compacts after sintering at 1150ºC were shown in Figure 2. The XRD patterns revealed information about the different crystalline phases with increasing the NCS-B contents. All compacts showed the presence of the akermanite (PDF #74-0990), while the composite of AK*x*/NCS-B*y* (*y*=20, 40, 60) showed one additional crystalline phase which is attributed to $Na_2Ca_2Si_3O_9$ (PDF #22-1455). With the composite proportion varying orderly, the relative intensity of the characteristic XRD peaks of akermanite decreased and simultaneously that for $Na_2Ca_2Si_3O_9$ increased. Moreover, it should be mentioned that no phosphate crystalline phases and calcium borate in the ceramic composition could be detected by XRD, mainly due to their low contents in the glass matrix.

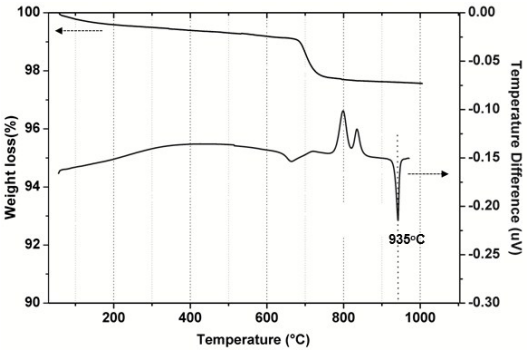

Figure 1. TG-DTA analysis of the as-prepared NCS-B powders.

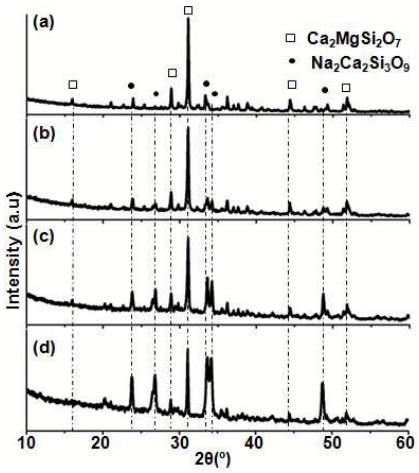

Figure 2. XRD patterns of the AKx/NCS-By compacts sintered at 1150°C.

3.3 Surface and fracture morphologies of AK*x*/NCS-B*y* ceramics

The surface morphology and fracture microstructure of the AK*x*/NCS-B*y* compacts were then investigated systematically by SEM observation. Figure 3 shows the SEM images of the typical AK*x*/NCS-B*y* samples after sintering at 1150°C. As for the AK100/NCS-B0, the shape of particles in the surface layer almost remained unchanged. However, the composite samples showed grain growth possibly due to the fluidizing of melted glass particles with increasing NCS-B content from 20% to 60%, and thus it could not be seen the loosely bonded grains in the surface layer of AK40/NCS-B60.

The effects of chemical composition on the fracture microstructure of AKx/NCS-By compacts can be observed from Figure 4. The presence of widespread closed pores with the increase of NCS-B content in the composites was observed. High density of closed pores were present in the cross-section of the AK40/NCS-B60 (1050, 1100, 1150°C), and the pore size was very large, ranging from submicron to several microns. All

of NCS-B-rich ceramics presented a modified densification and the fracture was predominantly transgranular. In particular, the AK80/NCS-B20 and AK60/NCS-B40 (1050, 1100°C) showed a denser structure with only very limited closed pores. In contrast, the AK100/NCS-B0 discs show high density of irregular open pores in the facture structure probably due to under-sintering.

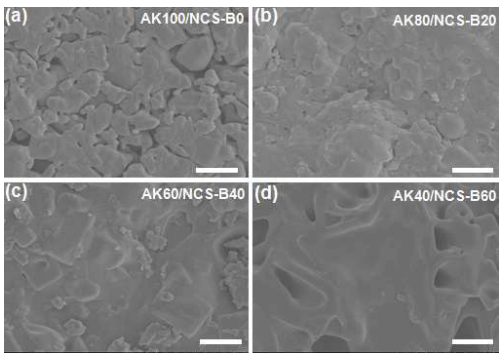

Figure 3. SEM images of the surface morphology of AKx/NCS-By compacts sintered at 1150°C. Bar: 20 μm.

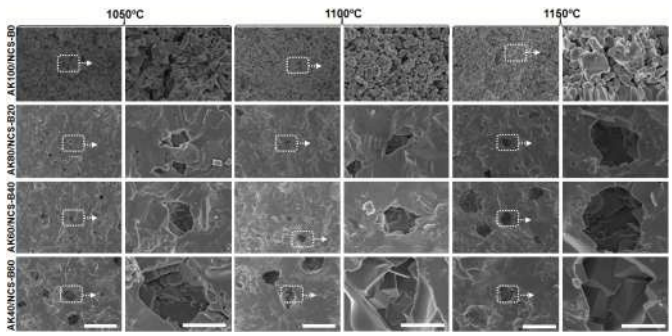

Figure 4. SEM micrographs of the cross-sectional microstructures of the AKx/NCS-By compacts after bending strength test. The bar represents 20 μm (short) and 5 μm (long).

3.4 Mechanical strength of AK*x*/NCS-B*y* compacts

The porosity of AK*x*/NCS-B*y* compacts was summarized in Table 1. Evidently, the AK100/NCS-B0 (≤1150°C) showed significant high amount of open pores (from 10.8±2.7% at 1000°C to 5.1±1.3% at 1150°C), while porosity of the AK80/NCS-B20 and AK60/NCS-B40 (1050°C, 1100°C) were below 3.0%, implying a markedly high densification for the laters. Interestingly, the porosity of AK40/NCS-B60 increased with the increase of sintering temperatures (1050–1150°C). This result suggests an overhigh content of NCS-B in the composites would lead to significant liquid-phase sintering, and thus negatively affect the densification of the AK*x*/NCS-B*y* composites.

Figure 5 shows the compressive and flexural strength of the AK*x*/NCS-B*y* ceramics sintered at 1000–1150°C. It can be seen that the AK80/NCS-B20 (1050°C) and AK60/NCS-B40 (1100°C) showed 1.5 times higher compressive strength (>220 MPa) than the pure akermanite (i.e. AK100/NCS-B0; Fig. 5a). However, the AK40/NCS-B60 (1150°C) showed a markedly strength decay (~47 MPa), and the average compressive strength (160~170 MPa) of AK80/NCS-B20 and AK60/NCS-B40 (1150°C) were nearly 5 times higher than that of the AK100/NCS-B0 (~36 MPa). As for the flexural strength (Fig. 5b), the maximum strength was nearly 100 MPa for the AK80/NCS-B20 (1100°C). This value was nearly ten times higher than the AK100/NCS-B0 sintered at the same temperature. Meanwhile, the AK80/NCS-B20 and AK60/NCS-B4 showed an increase in flexural strength when sintered at 1000−1100°C. The AK80/NCS-B20 (1150°C) exhibited considerable high flexural strength which was three-fold higher than the AK100/NCS-B0 (1150°C). In contrast, the AK100/NCS-B0 exhibited very limited flexural strength (<35 MPa). These mechanical data suggest that appropriate amount of NCS-B (e.g. 20%–40%) may readily reinforce the akermanite-based dense bioceramics when sintering at 1050–1100°C.

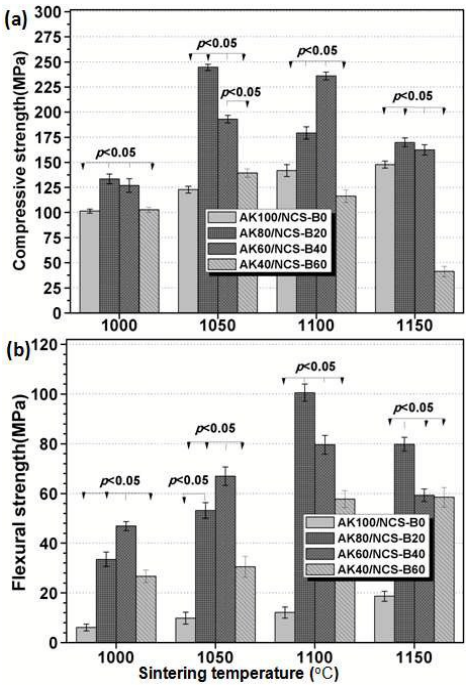

Figure 5. The compressive and flexural strength of AKx/NCS-By compacts sintered at different temperatures.

3.4 CHA formation ability on the ceramic composites

Figure 6 shows SEM micrographs of the AKx/NCS-By discs after immersion in SBF. After immersion for 1 and 4 d, respectively, it was occasionally observed that some globular structures precipitate on the surface of the samples containing ≤40% NCS-B, which might be identified as the first Ca-phosphate nuclei. All of sample surface was completely covered by a continuous coating layer with the typical CHA morphology after immersion in SBF for 7 d. EDX spectra (Fig. 6, inset) for the AK100/NCS-B0 and AK40/NCS-B60 showed that the chemical composition of the surface layer slightly differed in Ca/P ratio after 4 and 7 d of immersion in SBF, and the Ca/P ratio at 7 d (~1.43–1.66) was similar to that in calcium-deficient CHA.

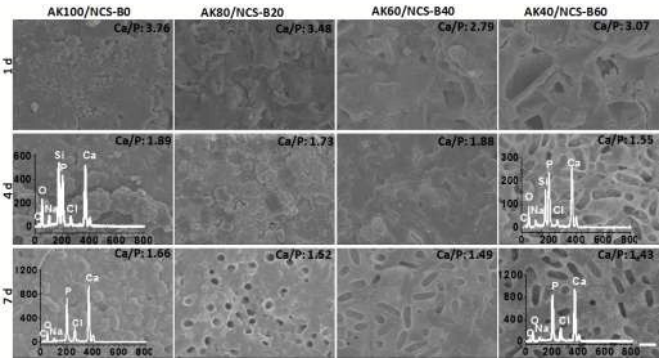

Figure 6. SEM images of the 1100°C-sintered AK*x*/NCS-B*y* compacts after immersion in SBF for 1-7 d. Insets showing the face-scanning EDX spectra of coating layer. Ca/P ratio was measured by EDX analysis. Bar: 1 μm.

Figure 7 shows the change of Ca, P, Si, and Mg concentrations in SBF during soaking of the AKx/NCS-By discs. The B concentration changed very slowly but was consistent with the boron content in the composites (Not shown). Appreciable differences for Ca and P concentrations were observed for the four groups within 48 h, but there followed a similar trend in ion concentrations. For the AK100/NCS-B0, the P and Si concentrations in SBF increased rapidly within 6 h and then P decreased abruptly. As for the AK40/NCS-B60, the Ca, Si and Mg concentrations gradually increased and then stabilized at a certain value, but P concentration experienced an increased and then decreased rapidly within 168 h, implying a fast CHA deposition during the early stage of the immersion in SBF. For the AK80/NCS-B20 and AK60/NCS-B40, the P concentration had a similar trend showing a high increase within 12 h, followed by a moderate decrease to 168 h. Moreover, Ca concentration also increased firstly and then changed mildly.

3.5 Biodissolution *in vitro*

Figure 8 shows that the weight loss of the AK*x*/NCS-B*y* ceramics sintered at 1100°C was similar to each other after 7 d (~2.4%) , 28 d (~5.2%), and 56 d (~7.6%) of immersion time,

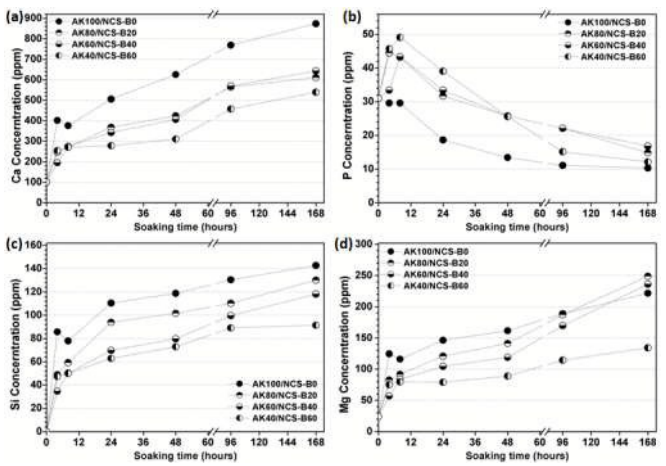

Figure 7. Changes in Ca (a), P (b), Si(c), and Mg (d) concentration in SBF during soaking the AKx/NCS-By compacts sintered at 1100°C.

whereas the weight loss of AK100/NCS-B0 in Tris buffer increased significantly with increasing the time. The pure akermanite showed a weight loss of 6.6%, and ~11% after immersing for 28 and 56 d, respectively. Meanwhile, the biodissolution rate of all AKx/NCS-By groups sintered at 1050°C also showed similar tendency but only displayed a slightly faster weight loss (Not shown), probably due to a looser structures in the ceramics.

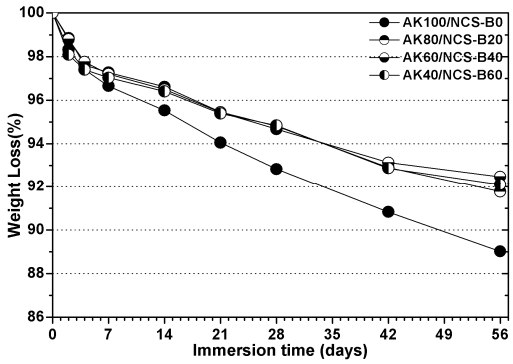

Figure 8. Weight loss of the AK*x*/NCS-B*y* compacts sintered at 1100°C after immersion in Tris buffers for different time periods.

3.6 Structural characteristic of 3D printed AK*x*/NCS-B*y* scaffolds

According to the quantitative analyses for the scaffold structure parameters, it was displayed that the strut thickness, pore size and porosity were slightly decreased with increasing NCS-B content and sintering temperature from 1050°C to 1100°C (Not shown). Specifically, the AK80/NCS-B20 and AK60/NCS-B40 (1100°C) exhibited significantly appreciable pore size (~327−340 μm) and open porosity (62−65%) than those of the AK40/NCS-B60 sintered at the same temperature. These quantitative analyses suggest the more is the NCS-B content, the higher is the shrinkage of the ceramic scaffolds during the sintering process.

Figure 9(a, b) shows the optical images of the as-sintered scaffolds. The ceramic scaffolds had a uniform structure with well regular pore morphology. There were no markedly changes in the microstructure along the length of the ceramic ink filaments. So each fracture surface would, in general, be representative of the whole construct. It is seen from the SEM images (Fig. 9c-f, inset) that the sintering process only improved the densification of the filament while avoiding deformation of the pore structure. Instead of nearly rectangular pores in the AK100/NCS-B0 scaffolds, incorporation of NCS-B resulted in rectangular- to-round corner transformation around the pore with increasing sintering temperature, implying the liquid-phase sintering in the ceramics. At 1100°C, the shape of particles in AK100/NCS-B0 almost remained unchanged (Fig. 9c). In comparison, the micrographs of these ceramic particles show softening while beginning to bond to each other (Fig. 9d, e). With increasing NCS-B up to 60% (e.g. AK40/NCS-B60; Fig. 9f), it appeared that the small pores or pits in the ceramic strut surface were hardly noticeable when sintering at 1100°C.

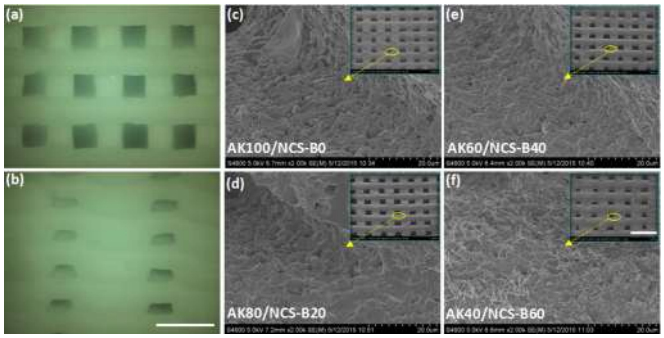

Figure 9. Optical images of the top- and side-view (a,b) and SEM images (c-f) of the fracture surface of the AKx/NCS-By scaffolds after sintering at 1100°C. The bar represents 800 μm (optical images) and 1mm (Inset SEM images).

3.7 Mechanical properties of 3D printed AKx/NCS-By scaffolds

The effect of sintering temperature and NCS-B content on the compressive strength and porosity of macroporous scaffolds is shown in Figure 10. Totally, the strength (in the direction parallel to the pore channel) increased from AK100/NCS-B0 to AK60/NCS-B40, and then decreased to AK40/NCS-B60. The AK80/NCS-B20 and AK60/NCS-B40 scaffolds sintered at 1050°C showed appreciable strength (19~36 MPa) than those sintered 1100°C. Furthermore, these strength values for the scaffolds sintered at 1050°C were respectively nearly 6 and 10 times higher than the AK100/NCS-B0 (1050°C), though the open porosity of the later was only higher by ~2.8% than the AK80/NCS-B20 and AK60/NCS-B40 composite scaffolds. Moreover, it should be mentioned that the compressive strength and porosity of the porous scaffolds were slowly decreased and increased, respectively, with prolongation of immersion time. The AK60/NCS-B40 scaffolds (1050°C) still had a compressive strength of ~25 MPa after 4 weeks. It suggests the 3D-printed macroporous scaffolds possess excellent mechanical stability.

4. Discussion

Biphasic hybrid, especially the *low melt-point* phase-assisted sintering, is a widely applied technological process in ceramic science that involves incorporating the secondary phase of appropriate compositions with low melt-point into the substrate to yield hybrid materials with desirable properties and functions[18]. For inorganic bioactive ceramics and glass-ceramics, secondary phase-assisted sintering is of fundamental importance in stabilizing a specific crystallographic phase, modifying mechanical properties, modulating sintering behavior as well as tuning biological performances. In this study we described a BG-reinforced akermanite and to give simultaneous control over the biodegradation and micro-structures of the (macroporous) ceramics. We showed that akermanite ceramic could be rationally tuned in phase component ($Ca_2MgSi_2O_7$–$Na_2Ca_2Si_3O_9$) and mechanical parameters through the usage of highly bioactive, low melt-point NCS-B at a defined concentration range.

The previous studies have shown that the flexural strength of akermanite ceramic was <40 MPa when pressureless sintering

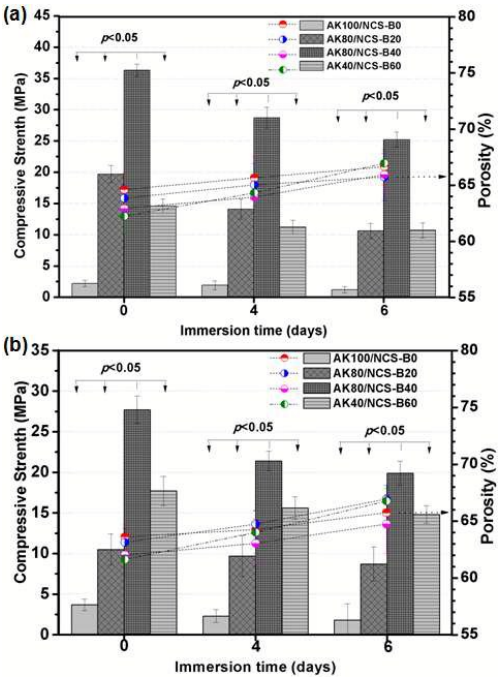

Figure 10. Changes in compressive strength and porosity of the 3D printed AKx/NCS-By scaffolds sintered at 1050°C (a) and 1100°C (b) before and after immersion in SBF.

at below 1200°C[19]. In this study, it is seen that the NCS-B-assisted sintering approach can significantly enhance the flexural strength (over 8 times) of akermanite ceramics at a very low sintering temperature level (e.g. 1100°C). The flexural strength (85–100 MPa) of the AK80/NCS-B20 (1100°C) is significantly optimized (Fig. 5b), which better match with the bone tissue (flexible strength: 50–150 MPa) compared with other low-temperature sintered Ca-Mg-silicate ceramics[20]. Meanwhile, the AK80/NCS-B20 and AK60/NCS-B40 ceramics (1050, 1100°C) show extremely high compressive strength (Fig. 5a), superior to the lower limit reported for cortical bone, and especially their strength value in compression of the porous formulation is over twice than that of other stoichiometric Ca-Mg silicate porous ceramics[21-23], calcium phosphates[24,25], and ten and seven times higher than the pure akermanite scaffolds fabricated respectively by ceramic ink writing in this study and laser sintering in the document[26]. Shuai's group have developed some laser-sintered Ca-/Ca-Mg silicate-based scaffolds via incorporation of the secondary phase such as boron nitride, nano-titania, silicon carbide, and graphene[21,22,27,28]. Unfortunately, the potential long-term effects in living body of these bio-inert additives is still unknown. In comparison, this study provides a reliable strategy that the addition of highly biocompatible and bioactive low-melt NCS-B is beneficial in improving mechanical properties with respect to the as-known inert phase or foreign ion doping routes.

According to previous studies, with the decrease of MgO content, the mechanical strengths of stoichoimetric monticellite, akermanite, and merwinite ceramics decreased[29]. It is indicated that Mg plays an important role in affecting the mechanical properties of bioceramics in the Ca-Mg silicates, and the

mechanical properties of bioceramics in this system may be controlled by adjusting the Mg content. On the other hand, additions of BG, alone and with other metal oxides in various combinations, have been used to promote the densification of structural bioceramics[6-8,30,31]. The presence of the specific BG additives in ceramic powder compacts is believed to provide a liquid phase at sintering temperatures by reaction with other components from the ceramic grain surfaces[32,33]. Presence of BG causes obvious signs of discontinuous grain growth which accounts for the decrease of residual porosity and the relatively high strength.

In general, the pure akermanite ceramic should be sintered at above 1300°C to obtain appropriate mechanical strength[19]. In fact, the laser sintered akermanite scaffolds also showed very poor strength even if a high temperature sintering was carried out[22]. These investigation indicate that, therefore, the optimal sintering temperature for the AK*x*/NCS-B*y* (porous) ceramics does not only satisfy the presence of liquid phase in the composites, but the temperature is also helpful for the densification of the akermanite phase. In this regard, we found that the NCS-B aid could significantly reinforce the mechanical strengths of the dense or porous AK*x*/NCS-B*y* ceramics at 1050–1100°C (Fig. 4). This is evidently attributed to the part liquid-phase sintering in the composite ceramics. To our knowledge, our study is an important attempt to confirm the incorporation of low-melt BG on the mechanical evolution of Ca-Mg silicate bioceramic system. It is known that the borate BG is lower melt point than that of the silicate BG[34]. In view of this, it can be seen from the present results that the appropriate amount of NCS-B occupy the interface of the akermanite grains in the dense compacts or pore struts, the ceramics exhibit more dense structure and higher strength. Accordingly, the NCS-B in akermanite readily improves the sintering behavior, structural densification, and mechanical strength of the (porous) ceramics.

On the other hand, because grain growth and phase conversion of low-melt BG are very sensitive to sintering temperature, liquid-phase sintering of low melt-point BG-rich products usually occurs at temperatures below 1200°C. Abnormal grain growth in low melt-point BG would occur in the final stage of densification if sintering temperature is too high, which has a great influence on flexural strength with increasing grain size. For pure akermanite ceramic, it has poor sinterability and is difficult to obtain dense sintering body below 1200°C, which leads to very poor flexural strength (<50 MPa). In contrast, the microstructure property of AK80/NCS-B20 and AK60/NCS-B40 ceramics sintered at 1050–1100°C have demonstrated that the small amount of NCS-B (≤40%) readily contributes to assisting sintering. The densification of AK*x*/NCS-B*y* ceramics is apparently influenced by sintering temperature and NCS-B, and especially the sintering densification is easily achieved in the AK*x*/NCS-B*y* ceramics. This is confirmed by the ultrahigh relative density (>97%) for AK80/NCS-B20 and AK60/NCS-B40 (1050, 1100°C) and appreciable value (>96%) for AK40/NCS-B60 (1050, 1100°C). As a result, the compressive strength and flexible strength of AK*x*/NCS-B*y* ceramics were both significantly enhanced with incorporation of NCS-B up to 20~40% (Fig. 5). In general, the relative density and average crystal size of ceramics significantly affects the mechanical properties[35]. High sintering temperatures of low-melt point BG often result in extreme grain coarsening and flaw structure[36]. This is also evidenced in the AK40/NCS-B60 (1050, 1100°C), where the ceramic fracture surface shows significant difference. Increase in sintering temperature up to 1150°C causes the small pores disappeared as a result of crystal-boundary migration and grain growth, which may explain the decrease of mechanical strength of (porous) AK40/NCS-B60. Moreover, the densification of the composite bioceramics is also affected by some other factors including grain morphology, grain size and thermal expansion coefficient of biphasic ceramics, and these factors probably influence the flexural strength and compressive strength. It is reasonable to assume that the porosity mainly affect the compressive strength, but the grain morphology and size contribute to the flexural strength. Therefore, it is difficult to obtain an optimized sintered temperature condition to endow highest compressive strength and flexural strength. Indeed, to get better mechanical strength, the optimum sintering temperature of AK80/NCS-B20 and AK60/NCS-B40 specimens is 1050−1100°C.

Previous studies have demonstrated that the CHA played an essential role in the maintenance of tissue-biomaterial interface, and this apatite layer could be reproduced in SBF[37]. In this study, the decrease in P concentrations in SBF after reaching maximum values indicates that such ions could be incorporated in the layer formed on the surface of the ceramics. However, the increase trend of Ca concentration as well as the decrease of P concentration in SBF within 4 d suggest that the solubility and apatite-formation ability of AK*x*/NCS-B*y* ceramics increase with increasing NCS-B content. The retardation in the apatite formation on the pure akermanite ceramics could be attributed to the influence of no P releasing to the solution that, as already reported, decreases the rate of formation of certain CaPs[38]. Our results obtained by SEM-EDX analysis showed that a calcium-deficient apatite layer fully covered the AK40/NCS-B60 surfaces after immersion for 4 d, but the AK100/NCS-B0 ceramics displayed a slight difference in apatite-formation ability. According to the mechanisms of nucleation and growth of biomimetic CHA on the inorganic biomaterials, the rate of apatite formation increased with the increase of material dissolution[39]. Hence, although the slight decrease in solubility of AK*x*/NCS-B*y* ceramics with adding NCS-B (Fig. 7), yet the existence of the highly bioactive $Na_2Ca_2Si_3O_9$, which is the crystalline phase of 45S5 BG-derived GC, readily promote the apatite mineralization rate (Fig. 6). Conversely, this is substantially favorable for overcoming the relatively fast dissolution rate of porous bioceramic that could compromise its mechanical strength *in vitro* and *in vivo*[40,41].

As demonstrated in our previous studies[17], NCS-B exhibits good low temperature sintering ability, and the higher NCS-B content in AK*x*/NCS-B*y* results in an increased densification, which leads to a slower ion leaching rate from the surface layer of the ceramics. Therefore, AK40/ NCS-B60 should be less biodissolution in aqueous solution and the leaching ion rate

should be lower (Fig. 7). Hence, with the increase of NCS-B content, the degradation rate decreased with the increase of the grain bonding from pure akermanite to AK40/NCS-B60 ceramic, resulting in the slower Ca ion release. This is also in agreement with the experimental results of weight loss of the biomaterials when immersing in Tris buffer (Fig. 8).

In addition, the biocompability of the akermanite have been validated by some previous studies[42]. Meanwhile, the 45S5 BG and some of borate-containing 45S5 GC analogues have also been demonstrated good biocompatibility and osteoconductive activity *in vivo*[43-45]. Moreover, the long-term interavenous administration studies have demonstrated that a CaO-SiO_2-P_2O_5-B_2O_3 GC showed no toxic effects to rats of either sex[46]. In this regard, it is reasonable to consider that the AK*x*/NCS-B*y* bioceramics would be highly cytocompatible due to its retarded ion release acceleration *in vitro* in comparison with the pure akermanite (Fig. 7). Also, the *in vivo* biological response of such mechanically strong porous constructs is expected since the evaluation of the spinal fusion animal model is under investigation and promises to yield more intriguing experimental results in the near future.

5. Conclusion

In summary, this investigation is demonstrated that a low-melt BG reinforcing approach can be used to modulate the mechanical and biological properties of the akermanite-based dense and porous bioceramic by the conventional pressureless sintering technique. In vitro SBF immersion experiments revealed that the appropriate amount (e.g. 40%) of NCS-B addition showed appreciable apatite formation ability similar to pure akermanite and the highly biocompatible BG reinforcement substantially contributed to the structural and strength reliability in such medium, which is particularly beneficial for enhancing osteogenic cell activity and bone regeneration. This finding suggests that our AK60/NCS-B40 porous scaffold is well suited to use in bone repair—for example, in *in situ* bone regeneration or in tissue engineering.

Acknowledgments

This work is supported by the National Science Foundation of China (81271956, 81301326, 51372218), the Zhejiang Provincial Natural Science Foundation of China (LZ14E020001, LQ14H060003), Science and Technology Department of Zhejiang Province Foundation (2015C33119, 2014C33202).

Notes

[a] Rui'an People's Hospital & the 3rd Affiliated Hospital to Wenzhou Medical University, Rui'an 325200, China. E-mail: Ygj.1008@163.com (Prof. G. Yang)

[b] Zhejiang-California International Nanosystems Institute, Zhejiang University, Hangzhou 310058, China. zhrgou@zju.edu.cn (Dr Z. Gou); Tel. +86 571-8820 8353.

[c] Institute of Advanced Manufacturing Engineering, Department of Mechanical Engineering, Zhejiang University, Hangzhou 310027, China.

[d] The First Affiliated Hospital, School of Medicine of Zhejiang University, Hangzhou 310003, China.

References

1 P. Weiss, P. Layrolle, L.P. Clergeau, B. Enckel, P. Pilet, Y. Amouriq, G. Daculsi, B. Giumelli, *Biomaterials,* 2007, **28**, 3295–3305.

2 M. Marcacci, E. Kon, V. Moukhachev, A. Lavroukov, S. Kutepov, R. Quarto, M. Mastrogiacomo, R. Cancedda, *Tissue Eng,* 2007, **13**, 947–955.

3 R. Quarto, M. Mastrogiacomo, R. Cancedda, S.M. Kutepov, V. Mukhache, A. Lavroukov, E. Kon, M. Marcacci, *N Engl J Med,* 2001, **344**, 385–386.

4 L.L. Hench, *J Am Ceram Soc,* 1991, **74**, 1487–1510.

5 L.L. Hench, *J Eur Ceram Soc,* 2009, **29**, 1257–65.

6 A. Winkel, R. Meszaros, S. Reinsch, R. Muller, N. Travitzky, T. Fey, P. Greil, and L. Wondraczek, *J Am Ceram Soc,* 2012, **95**, 3387-3393.

7 K.L. Lin, J Chang, Z.W. Liu, Y. Zeng, R.X. Shen, *J Eur Ceram Soc,* 2009, **29**, 2937-2943

8 K.L. Lin, S.Y. Ni, J. Chang, W.Y. Zhai, and W.M. Gu, *Key Eng Mater,* 2007, **330-332**, 181-184.

9 S. Xu, K. Lin, Z. Wang, J. Chang, L. Wang, J. Lu, C. Ning, *Biomaterials,* 2008, **29**, 2588–2596.

10 C. Wu, J. Chang, *J Biomed Mater Res B Appl Biomater,* 2007, **83B**, 153–160.

11 C.T. Wu, J. Chang, *J Biomat Appl,* 2006, **21**, 119-129.

12 H.L. Sun, C.T. Wu, K.R. Dai, J. Chang, T.T. Tang, *Biomaterials,* 2006, **27**, 5651–5657.

13 Y. Huang, X.G. Jin, X.L. Zhang, H.L. Sun, J.W. Tu, T.T. Tang, J. Chang, K.R. Dai, *Biomaterials,* 2009, **30**, 5041-5048.

14 D. Lin, Q. Nian, B.W. Deng, S.Y Jin, Y.W. Hu, W.Q. Wang and G.J. Cheng, *ACS Nano,* 2014, **8**, 9710–9715.

15 S. Bose, S. Vahabzadeh and A. Bandyopadhyay, *Mater Today,* 2013, **16**, 496-504.

16 N. Travitzky, A. Bonet, B. Dermeik, T. Fey, I. Filbert-Demut, L. Schlier, T. Schlordt and P. Greil, *Adv Eng Mater,* 2014, **16**, 729-745.

17 K. Xie, L. Zhang, X. Yang, G. Yang, X. Wang, L. Zhang, H. Shao, Y. He, J. Fu, Z. Gou, *Biomed Glasses,* 2015, **1**, 81-93.

18 J.R. Jones, *Acta Biomater,* 2013, **9**, 4457-4486.

19 C.T. Wu, J. Chang. *J Biomater Appl,* 2006, **21**, 119–129.

20 M. Diba, O.M. Goudouri, F. Tapia and A.R. Boccaccini, *Current Opin Solid State Mater Sci,* 2014, **18**, 147-167.

21 C.J. Shuai, C.D. Gao, P. Feng, S.P. Peng, *RSC Adv,* 2014, **4**, 12782–12788.

22 P. Feng, C.D. Gao, C.J. Shuai, and S.P. Peng, *RSC Adv,* 2015, **5**, 3498-3507.

23 C.T. Wu, J.A. Chang, W.Y. Zhai, S.Y. Ni, J.Y. Wang, *J Biomed Mater Res Part B,* 2006, **78B**, 47–55.

24 G.A. Fielding, A. Bandyopadhyay, S. Bose, *Dental Mater,* 2011, **28**, 113-122.

25 Liu, D.M, *Ceram Inter,* 1997, **23**, 135-139.

26 Z. Han, P. Feng, C. Gao, Y. Shen, C. Shuai, S. Peng, *Bio-Med Mater Eng*, 2014, **24**, 2073-2080.

27 C. Shuai, Z. Han, P. Feng, C. Gao, T. Xiao, S. Peng. *J Mater Sci: Mater Med,* 2015, **26**,188.

28 Z.K. Han, C.D. Gao, P. Feng, Y. Shen, C.J. Shuai and S.P. Peng, *RSC Adv,* 2014, **4**, 36868-36874.
29 X.C. Chen,J. Ou, Y. Wei, Z.B. Huang, Y.Q. Kang and G.F. Yin, *J Mater Sci: Mater Med,* 2010, **21**, 1463-1471.
30 M.A. Lopes, J.D. Santos, F.J. Monteiro, J.C. Knowles, *J Biomed Mater Res,* 1998, **39**, 244–251.
31 C. Bergmann, M. Lindner, W. Zhang, K. Koczur, A. Kirsten, R. Telle, H. Fischer, *J Euro Ceram Soc,* 2010, **30**, 2563–2567.
32 C.Y. Huang, Z.T. Zhang, Z.L. Tang, *J Mater Sci Lett,* 1999, **18**, 1815-1816.
33 X. Yu, S. Cai, G. Xu, W. Zhou, D. Wang, *J Mater Sci: Mater Med,* 2009, **20**, 2025-2034.
34 H. Segawa, T. Igarashi, T. Sakamoto, K. Mizuno, T. Konishi, S. Inoue, *Int j Appl Glass Sci,* 2010, **1**, 378-387.
35 R.W. Rice, *J Mater Sci,* 1996, **31**, 1969-1983.
36 L. Lin, L. Zhang, J Wang, K. Xie, X. yang, X. Chen, G. yang, C. Gao, Z. Gou, *Mater Lett*, 2014, **126**, 154-1458.
37 T. Kokubo, H. Kushitani, S. Saka, T. Kitsgi, T. Kitsugi and T. Yamamuro, *J Biomed Mater Res,* 1990, **24**, 721–734.
38 P. Ducheyne, S. Radin and L. King, *J Biomed Mater Res,* 1993, **27**, 25-34.
39 L.L. Hench, K.J. West, *Life Chem Reports,* 1996, **13**, 187-241.
40. C. Wu, J. Chang, W. Zhai, S. Ni, J. Wang, *J Biomed Mater Res B: Appl Biomater*. 2006, **78**, 47-55.
41. J. H. Lee, H.-S. Ryu, J.-H. Seo, D.-Y. Lee, B.-S. Chang, C.-K. Lee, *Clin Orthop Surg*, 2014, **6**, 87-95.
42. C. Chen, P. Watkins-Curry, M. Smoak, K. Hogan, S. Deese, G. T. McCandless, J. Y. Chan, D. J. Hayes. *ACS Biomater Sci Eng*, 2015, **1**, 94-102.
43. M. Hamadouche, A. Meunier, D. C. Greenspan, C. Blanchat, J. P. Zhong, G. P. La Torre, L. Sedel, *J Biomed Mater Res*, 2001, **54**, 560-566.
44. Z. Xie, X. Liu, W. Jia, C. Zhang, W. Huang, J Wang, *J Control Release*, 2009, **139**, 118-126.
45. J. H. Lee, C.-K. Lee, B.-S. Chang, H.-S. Ryu, J.-H. Seo, K.S. Hong, H. Kim, *J Biomed Mater Res*, 2006,**77A**, 362-569.
46. J. H. Lee, H.-S. Ryu, J.-H. Seo, B.-S. Chang, C.-K. Lee, *Drug Chem Toxicol*, 2010, **33**, 38-47.

TOC